mater.scichina.com link.springer.com

Published online 28 December 2020 | https://doi.org/10.1007/s40843-020-1531-7
Sci China Mater 2021, 64(5): 1114–1126

Efficient reversible CO/CO_2 conversion in solid oxide cells with a phase-transformed fuel electrode

Yihang Li[1,2], Manish Singh[3], Zechao Zhuang[4], Yifu Jing[1], Fengjiao Li[1], Kristina Maliutina[1], Chuanxin He[1] and Liangdong Fan[1,5*]

ABSTRACT **The reversible solid oxide cell (RSOC) is an attractive technology to mutually convert power and chemicals at elevated temperatures. However, its development has been hindered mainly due to the absence of a highly active and durable fuel electrode. Here, we report a phase-transformed CoFe-$Sr_3Fe_{1.25}Mo_{0.75}O_{7-\delta}$ (CoFe-SFM) fuel electrode consisting of CoFe nanoparticles and Ruddlesden-Popper-layered $Sr_3Fe_{1.25}Mo_{0.75}O_{7-\delta}$ (SFM) from a $Sr_2Fe_{7/6}Mo_{0.5}Co_{1/3}O_{6-\delta}$ (SFMCo) perovskite oxide after annealing in hydrogen and apply it to reversible CO/CO_2 conversion in RSOC. The CoFe-SFM fuel electrode shows improved catalytic activity by accelerating oxygen diffusion and surface kinetics towards the CO/CO_2 conversion as demonstrated by the distribution of relaxation time (DRT) study and equivalent circuit model fitting analysis. Furthermore, an electrolyte-supported single cell is evaluated in the 2:1 CO-CO_2 atmosphere at 800°C, which shows a peak power density of 259 mW cm^{-2} for CO oxidation and a current density of −0.453 A cm^{-2} at 1.3 V for CO_2 reduction, which correspond to 3.079 and 3.155 mL min^{-1} cm^{-2} for the CO and CO_2 conversion rates, respectively. More importantly, the reversible conversion is successfully demonstrated over 20 cyclic electrolysis and fuel cell switching test modes at 1.3 and 0.6 V. This work provides a useful guideline for designing a fuel electrode through a surface/interface exsolution process for RSOC towards efficient CO-CO_2 reversible conversion.**

Keywords: reversible solid oxide cells, CO-CO_2 conversion, perovskite oxide, phase transformation, cyclic test

INTRODUCTION

The demand for utilization and storage of renewable energy has been rapidly growing for decades as a result of the depletion of fossil fuels and fear of CO_2 emission. However, the nature of intermittency and variability makes only a small percentage of these energy systems available. To achieve a sustainable system, it is critical to develop energy conversion and storage technologies for clipping peak (shifting electricity from peak periods to off-peak periods), e.g., mountain water reservoirs, batteries, and reversible solid oxide cell (RSOC) systems [1,2].

Among all, RSOC has proven to be a highly effective technology for this purpose [3]. It can be reversibly operated by using CO_2 and H_2O electrolysis to CO and H_2 (chemical energy carriers) in the solid oxide electrolysis cell (SOEC) mode and converting it back to generate electricity under the solid oxide fuel cell (SOFC) mode [4–6]. However, the development of RSOC remains a challenge due to many limitations. In particular, the electrochemical performance and durability are largely limited by the fuel electrode reaction instead of the oxygen electrode reaction, as expressed by Equations (1) and (2) using Kröger-Vink notations:

Fuel electrode

$$CO_2+2e'+V_O^{\bullet\bullet} \underset{\text{SOFC}}{\overset{\text{SOEC}}{\rightleftarrows}} CO+O_O^{\times}, \quad (1)$$

Oxygen electrode

$$O_O^{\times} \underset{\text{SOFC}}{\overset{\text{SOEC}}{\rightleftarrows}} \frac{1}{2}O_2+2e'+V_O^{\bullet\bullet}, \quad (2)$$

where $O_O^{\times}$ is an oxygen atom on the oxygen site with no

[1] College of Chemistry and Environmental Engineering, Shenzhen University, Shenzhen 518060, China
[2] College of Physics and Optoelectronic Engineering, Key Lab of Optoelectronic Devices and Systems of Ministry of Education/Guangdong Province, Shenzhen University, Shenzhen 518060, China
[3] Department of Chemistry, Division for Pure and Applied Biochemistry, Naturvetarvägen 14, 22362, Lund University, Sweden
[4] Department of Chemistry, Tsinghua University, Beijing 100084, China
[5] Shenzhen Key Laboratory of New Lithium-ion Batteries and Mesoporous Materials, Shenzhen University, Shenzhen 518060, China
* Corresponding author (email: fanld@szu.edu.cn)

charge relative to the lattice, and $V_O^{\cdot\cdot}$ is a vacancy on the oxygen site with two positive charges. The well-established Ni-YSZ (Y_2O_3 stabilized ZrO_2) fuel electrode is susceptible to degradation caused by coking and poisoning when it is used for CO-CO_2 conversion in RSOC, especially under the SOEC mode [7–10]. Ebbesen *et al.* [11] reported the rapid passivation of Ni-YSZ supported cells for CO_2 reduction under the SOEC mode. It could not be fully recovered when operated under the SOFC mode to oxidize carbon. The addition of water steam for the CO_2-H_2O coelectrolysis was proposed by Yan *et al.* [12], but this addition will increase the cost of the RSOC system during operation.

Recently, perovskite materials with mixed ionic and electronic conducting properties have been explored as alternative electrodes due to their excellent redox stability and high resistance to carbon deposition in the absence of water. For example, La(Sr)Cr(Mn)$O_{3-\delta}$ [13,14], (La)$SrTiO_{3+\delta}$ [15], and several Fe-based materials [16] are most commonly studied. Unfortunately, the obtained electrochemical performances remain inferior compared with the Ni-YSZ composite [17]. Some studies have shown that the performance can be improved by introducing metal nanoparticles on the perovskite surface through various deposition techniques such as vapor deposition, infiltration, and exsolution [18–22].

Metal/alloy nanoparticles, which are *in situ* exsolved from perovskite oxide bulk to the surface, have gathered a considerable amount of interest because of their desired phase dispersion, strong aggregation and coking-resistance properties [23–28]. Typically, various reducible metal cations are incorporated into the B-site of the perovskite lattice in the oxidizing atmosphere and subsequently exsolved as metallic nanoparticles on the perovskite surface under reducing conditions. Fig. 1 depicts a Cartesian plot of visual distinction for different chemical compositions and crystal structures upon the exsolution of B-site metals, where there are O-site and A-site nonstoichiometry as the *x*- and *y*-axes, respectively, and defect-free ABO_3 as the origin. For an initially nonstoichiometric ABO_3 (i.e., A/B<1), the A-site deficiency can facilitate the diffusion of B-site cations for the exsolution process. For example, in the second quadrant, Neagu *et al.* [29] reported that Ni nanoparticles exsolved from $La_{0.8}Ce_{0.1}Ni_{0.4}Ti_{0.6}O_{3+\delta}$ achieved large populations and exhibited superior catalytic activity and stability for the CO oxidation reaction. For an initial stoichiometric ABO_3 (i.e., A/B=1) perovskite, the exsolution of B-site cations can result in the formation of Ruddlesden-Popper (R-P) oxide phase *via* phase transformation. In the first quadrant, Liu *et al.* [30] reported that CoFe alloy nanoparticles were exsolved from $Pr_{0.4}Sr_{0.6}Co_{0.2}Fe_{0.7}Mo_{0.1}O_{3-\delta}$ with the formation of $(Pr_{0.4}Sr_{0.6})_3(Fe_{0.85}Mo_{0.15})_2O_7$ with the R-P layered structure, which enhanced the CO_2 electrolysis performance in SOEC. Similar results were also reported for SOFC using hydrogen or hydrocarbon fuels [31,32], which highlighted excellent resistance to carbon deposition and sulfur poisoning. Hence, this exsolution strategy will highly likely play a significant role in RSOC for the CO/CO_2 conversion, which has not been reported in the literature to the best of our knowledge.

Remarkably, Fe-based perovskites demonstrate the desired conductivity, high redox stability, and acceptable electrocatalytic activity. Inspired by these insights, we designed an Fe-rich perovskite $Sr_2Fe_{7/6}Mo_{0.5}Co_{1/3}O_{6-\delta}$

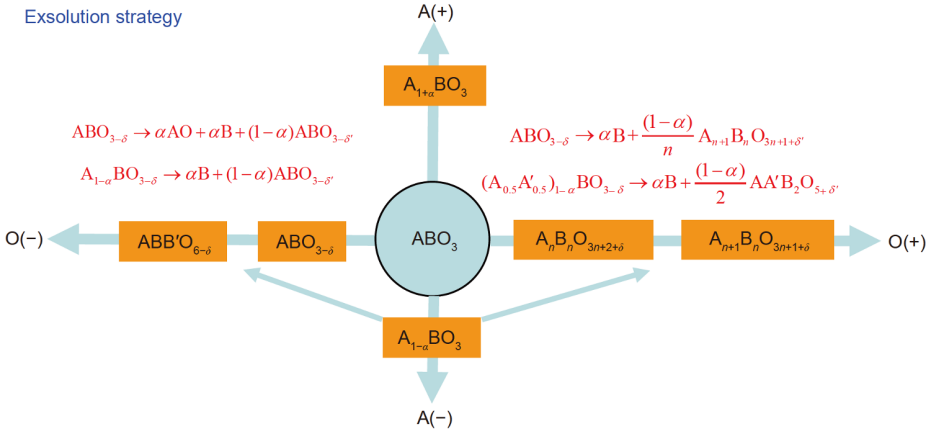

Figure 1 Cartesian plot that anticipates the key role of perovskite nonstoichiometry for the *in situ* exsolution process, where the *x*- and *y*-axes correspond to oxygen-site and A-site nonstoichiometry, respectively. Deficiency and excess are indicated by (−) and (+), respectively.

(SFMCo), which is phase-transformed into CoFe alloy and R-P layer-structured $Sr_3Fe_{1.25}Mo_{0.75}O_{7-\delta}$ (SFM) composite after being annealed in hydrogen. In this work, this novel material is used as the fuel electrode to facilitate the CO/CO_2 conversion kinetics and enhance the resistance against carbon deposition in RSOC. Furthermore, we evaluated the electrochemical performance of RSOC with this fuel electrode and demonstrated the reversible operation under cyclic SOFC and SOEC modes.

EXPERIMENTAL SECTION

Powder preparation

SFMCo powders were synthesized using a conventional citric-glycine combustion method. Stoichiometric amounts of chemicals $Sr(NO_3)_2$, $Fe(NO_3)_3{\cdot}9H_2O$, $(NH_4)_6Mo_7O_{24}{\cdot}4H_2O$ and $Co(NO_3)_2{\cdot}6H_2O$ (all from Sinopharm Chemical Reagent Co., Ltd) were dissolved in deionized water using citric acid and glycine as complexing agents. By evaporating *via* a stove plate, a dark purple gel was obtained. Then, the gel was calcined at 1000°C for 5 h to obtain SFMCo powders. The reference sample $Sr_2Fe_{1.5}Mo_{0.5}O_{6-\delta}$ (P-SFM) was synthesized using the same method. After annealing in a quartz tube under flowing hydrogen at 800°C for 2 h, SFMCo samples were transformed into CoFe alloy and R-P layer-structured $Sr_3Fe_{1.25}Mo_{0.75}O_{7-\delta}$ (CoFe-SFM for short). $Sm_{0.2}Ce_{1.8}O_{2-\delta}$ (SDC) powders were synthesized by the coprecipitation method [33]. $(La_{0.85}Sr_{0.15})_{0.9}MnO_{3-\delta}$ (LSM) powders were synthesized by the glycine combustion [34]. $(Y_2O_3)_{0.08}(ZrO_2)_{0.92}$ (YSZ, Fuel Cell Materials, USA) powders were used without further treatment as the electrolyte.

Fabrication of the symmetrical cells and single cells

The symmetrical cell was composed of one YSZ electrolyte substrate, two electrode layers, and two SDC buffer layers between the electrolyte and electrode. Dense YSZ electrolyte substrates (~200 μm in thickness) were prepared by dry pressing powders under ~400 MPa and subsequent sintering at 1450°C for 5 h in air. An SDC layer was screen-printed onto both sides of the YSZ surface and sintered at 1200°C for 3 h. In addition, the SFMCo layer was screen-printed onto the SDC surface and sintered at 1000°C for 2 h. For the single cell with the SFMCo/SDC//YSZ//LSM-SDC configuration, the LSM-SDC (6:4 in the mass ratio) layer was screen-printed onto the other surface of YSZ and subsequently calcined at 1200°C for 2 h. Ag (current collector) paste was deposited onto the SFMCo and LSM-SDC surfaces and heat treated at 500°C for 1 h.

Characterization methods

X-ray diffraction (XRD) analyses were conducted using a Rigaku TTR-III diffractometer with a Cu Kα radiation source. High-resolution transmission electron microscopy (HRTEM) and the corresponding energy dispersive X-ray (EDX) mapping analyses were performed on a JEOL JEM-F200 TEM/STEM. X-ray photoelectron spectroscopy (XPS, ESCALAB 250) was used to investigate the chemical states of the elements. The microstructures of the cells and their electrodes were analyzed using field emission scanning electron microscopy (FE-SEM, JEOL JSM7000F). H_2 temperature-programmed reduction (H_2-TPR) experiments were performed using TPDRO 1100 from 40 to 800°C. Symmetrical cells were investigated at 700–850°C under 2:1 $CO\text{-}CO_2$ (P_{O2} = 9.49×10^{-20} atm at 800°C) atmosphere.

Electrochemical performance measurement

The electrochemical impedance spectroscopy (EIS) was conducted in the frequency range of 0.01–1 MHz (Solarton 1260) under open-circuit voltage (OCV) conditions. Single cells were sealed on an alumina tube using conductive resins. Before the test, the fuel electrode was annealed in hydrogen at 800°C for 2 h, and the LSM-SDC oxygen electrode was exposed in ambient air. Afterward, the feeding gas was switched to 2:1 $CO\text{-}CO_2$ at a flow rate of 50 mL min^{-1}. Polarization characteristics (*I-V* curves) and EIS of single cells were measured through a two-electrode configuration using Solarton 1287 & 1260. The distribution of relaxation time (DRT) method was applied to deconvolute EIS using DRT tools from Francesco's group [35,36], where the regularization parameter was set to 10^{-3}.

RESULTS AND DISCUSSION

The CoFe alloy exsolution process was accompanied by the phase transformation of the SFMCo perovskite parent. First, the corresponding reduction-exsolution temperature was analyzed by H_2-TPR, as shown in Fig. 2a. For reference sample P-SFM [37], the reduction of Fe^{n+} (n = 3 and 4) likely occurs in two main steps, i.e., the two peaks at 494°C and 526°C, which correspond to the reduction of $Fe^{4+}\rightarrow Fe^{3+}$ and $Fe^{3+}\rightarrow Fe^{2+}$. When Co is doped into P-SFM to form SFMCo, the first reduction peak is reduced to 447°C, and the second reduction peak is reduced to 499°C. Two additional overlapped peaks appear at 708 and 751°C, which should correspond to the reduction of Co^{n+} (n = 2, 3 and 4) into metallic Co^0 and Fe^{2+}

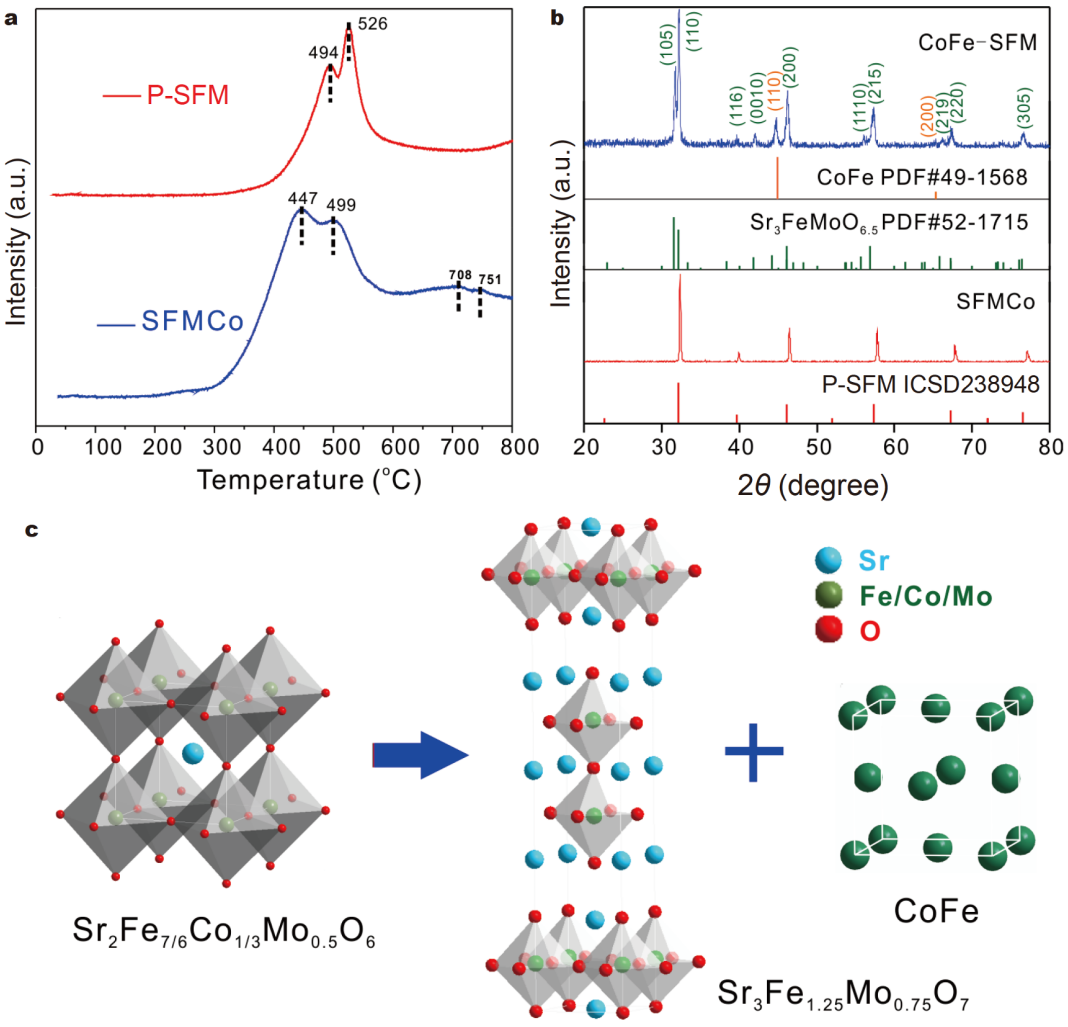

Figure 2 (a) H_2-TPR profiles of P-SFM [37] and CoFe-SFM samples; (b) XRD patterns of SFMCo and CoFe-SFM powders; (c) illustration model for the structural transformation of SFMCo (cubic) to SFM (tetragonal) and CoFe alloy (cubic).

into Fe^0, respectively. This process depicts the temperature window of exsolution and phase transformation from SFMCo into CoFe alloy and SFM. To remarkably facilitate this transformation process, the reduction temperature was set to 800°C and maintained for 2 h.

Fig. 2b shows the XRD patterns of the as-prepared SFMCo and reduced SFMCo powders. The SFMCo sample exhibits a cubic perovskite with the $Pm\bar{3}m$ space group like the isostructural P-SFM (ICSD-238948) [38], which implies that Co has been well doped into SFM perovskite without causing any structural change or formation of the secondary phase. After a reduction in H_2 at 800°C for 2 h, the pure perovskite phase is transformed into two different phases: an R-P phase and an alloy phase. The R-P phase can be well indexed with tetragonal $Sr_3FeMoO_{6.5}$ (PDF#52-1715), while the alloy phase corresponds to cubic CoFe alloy (PDF#49-1568). The above information reveals the feasibility of this strategy. Therefore, the phase transformation of SFMCo can be mathematically expressed as Equation (3), since all Co were exsolved from the SFMCo perovskite parent.

$$\mathrm{Sr_2Fe_{7/6}Mo_{0.5}Co_{1/3}O_{6-\delta}} \rightarrow \frac{1}{3}\mathrm{CoFe} + \frac{2}{3}\mathrm{Sr_3Fe_{1.25}Mo_{0.75}O_{7-\delta'}} + \left(\frac{2}{3}-\frac{1}{2}\delta+\frac{1}{3}\delta'\right)\mathrm{O_2}\uparrow. \quad (3)$$

Furthermore, Fig. 2c depicts the illustration model for the structural transformation of cubic SFMCo to tetragonal SFM and cubic CoFe alloy. As observed, SFM exhibits a type of R-P layered structure ($A_nB_nO_{3n+1}$, $n = 2$ in our case), where the [$Sr_2Fe_{1.25}Mo_{0.75}O_{6-\delta}$] perovskite layer and [Sr–O] rock-salt layer are alternately arranged along the *c*-axis. As suggested in other studies [32,39,40], these

materials show excellent thermal and structural stabilities.

The chemical compositions and microstructure were further investigated. Fig. 3a shows the distribution of elements for the CoFe-SFM sample under the high-angle annular dark field (HAADF) mode. Sr, Fe, Mo, Co, and O were found in CoFe-SFM. Unlike the uniform distribution of Sr, Mo and O elements, partial Fe (bright red) and almost all Co (bright green) have been exsolved from the perovskite oxide parent. Because they are at the same location, exsolved Co and Fe exist in the form of alloy (solid solution), which is consistent with the XRD analysis. As reported by Gao *et al.* [41], the exsolution process consists of four steps: cation diffusion, reduction, nucleation, and particle growth. In the case of SFMCo, first, Co and Fe cations diffuse from the bulk to the surface or near the surface; then, they were reduced to metallic Co^0 and Fe^0. Subsequently, the initially formed Co^0 and Fe^0 nuclei are combined into fine alloy nanoparticles through the local near-surface migration.

The detailed TEM image is shown in Fig. 3b. The dispersed CoFe nanoparticles in the range of 20–50 nm are socketed on the SFM substrate by being submerged near the surface. The resulting interface (a close curve) indicates the strong interaction between nanoparticles and perovskite oxide parents because the CoFe lattice is undeniably epitaxially grown from the perovskite oxide lattice [42]. Fig. 3c presents an enlarged view of the white rectangle in Fig. 3b to identify the lattice fringe orientation and interplanar spacing. The interplanar spacing of nanoparticles (orange rectangle) is 0.198 nm, which cor-

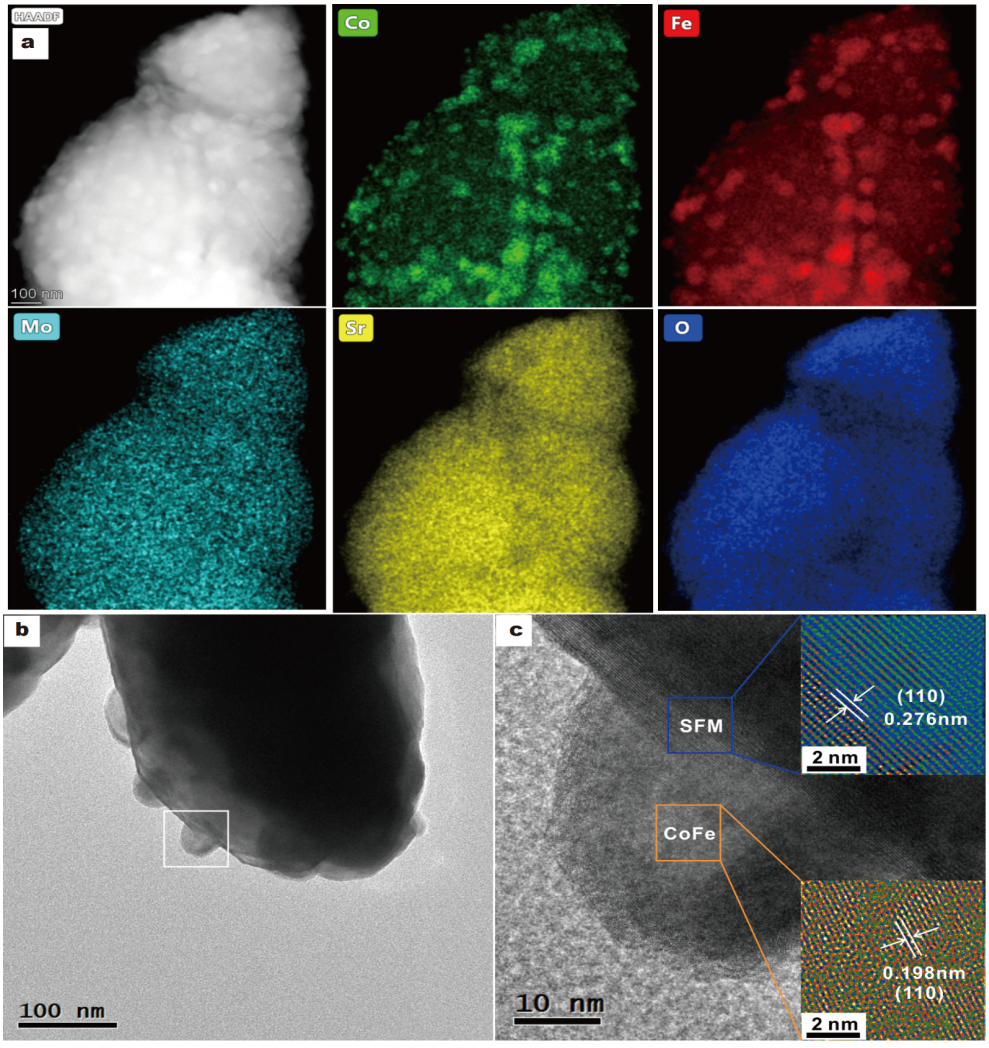

Figure 3 (a) HAADF image of CoFe-SFM powders and corresponding elemental mapping; (b) TEM image of a typical CoFe-SFM sample; (c) enlarged view of the white rectangle of b (Insets are HRTEM images of CoFe nanoparticles and SFM, respectively).

responds to the (110) planes of the CoFe alloy phase. The interplanar spacing of parent oxide (blue rectangle) is 0.276 nm, which is similar to the (110) planes of the SFM crystalline phase.

Oxygen vacancies are very crucial to electrode materials, which are required for oxygen ion transport from the electrode to the electrolyte. In addition, surface oxygen vacancies act as host sites for the adsorption and activation of CO/CO_2 molecules [43]. In this regard, XPS measurement was conducted to investigate the chemical state of oxygen species; and the results are shown in Fig. S1. Given Gaussian fitting, three binding energy components are observed in the CoFe-SFM sample (Fig. S1a), which are deconvoluted into a low-energy peak, a middle-energy peak, and a high-energy peak centered at 529.51, 531.17, and 532.63 eV, respectively. The low-energy peak comes from lattice oxygen ions (O_L, 1.95%) on the intrinsic sites. The middle-energy peak is attributed to undercoordinated oxygen-containing species (O_S, 74.93%), which is positively related to the oxygen vacancy concentrations [44]. Since SFM has a layer structure, which consists of a perovskite layer and a rock salt layer, the oxygen vacancies and interstitial oxygen (O_i'', 23.12%) ions can coexist in the SFM lattice, which are accommodated on octahedral sites and tetrahedral interstitial sites, respectively [45,46]. Based on this information, the high-energy peak is assigned to interstitial oxygen ions (O_i'') [47,48], which can be interpreted as the formation of an anion Frenkel-type defect on the oxygen sublattice as follows:

$$O_O^{\times} \rightarrow O_i'' + V_O^{\bullet\bullet}, \quad (4)$$

where O_i'' is an oxygen ion on an interstitial site with two negative charges. The [Sr–O] rock-salt layer contributes to O_i'' transport along the *a*-*b* plane by an interstitial (push-pull) mechanism between interstitial and apical oxygen sites from the $Fe(Mo)O_6$ octahedra, whereas the $[Sr_2Fe_{1.25}Mo_{0.75}O_{6-\delta}]$ perovskite layer with oxygen vacancies is responsible for the transport of lattice oxygen ions *via* 3-dimensional vacancies by the hopping mechanism [45]. The coexistence of these two types of defects is very favorable for the solid-gas oxygen exchange reaction and bulk oxygen ion diffusion in typical solid oxide cell conditions [49,50]. Unlike the CoFe-SFM sample, two binding energy components are only observed in the SFMCo sample (Fig. S1b), while O_L and O_S account for 53.23% and 46.77%, respectively. It should be noted that SFM-based material systems show an n-type conducting behavior in a reducing atmosphere [43]. During the phase-transformation process, the partial Fe cations are reduced to lower oxidation states when lattice oxygen is removed, which increases the concentrations of both oxygen vacancies and electrons as follows:

$$2Fe_{Fe}^{\times} + O_O^{\times} \rightarrow 2Fe_{Fe}'(e') + V_O^{\bullet\bullet} + \frac{1}{2}O_2, \quad (5)$$

where $Fe_{Fe}^{\times}$ is an Fe^{3+} cation on the Fe site with no charge relative to the lattice, and Fe_{Fe}' is an Fe^{2+} cation on the Fe site with a negative charge relative to the lattice. These positive effects are expected to improve the catalytic activity of the fuel electrode towards the CO/CO_2 conversion.

The electrochemical catalytic activities of the fuel electrode for the $CO\text{-}CO_2$ conversion reaction were investigated by EIS plots using YSZ-supported symmetrical cells (SFMCo/SDC/YSZ/SDC/SFMCo and CoFe-SFM/SDC/YSZ/SDC/CoFe-SFM) in a 2:1 $CO\text{-}CO_2$ atmosphere. SDC as the buffer layer was also significantly reduced, which results in a behavioral change of the pure ionic conductor to a mixed ionic-electronic conductor. Fig. 4a, b display the Nyquist plots of EIS for SFMCo and CoFe-SFM fuel electrodes at 700–850°C under OCV conditions. To intuitively compare the electrode polarization resistance (R_p), all first intercepts with *Z*'-axis were simplified to zero by subtracting the real ohmic resistance [51]. The difference between the two Z'-axis intercepts at the high frequency and low frequency of each impedance plot represents the R_p value. The R_p value reflects the catalytic activity towards the CO/CO_2 conversion reaction; a lower R_p value indicates a higher activity and *vice versa*. In Fig. 4a, the R_p values of the SFMCo fuel electrode are determined to be 0.687, 1.523, 3.475 and 8.402 $\Omega\,cm^2$ at 850, 800, 750 and 700°C, respectively. In contrast, the corresponding R_p values are reduced to 0.292, 0.750, 1.855, and 4.699 $\Omega\,cm^2$ for CoFe-SFM, which indicates better electrocatalytic activity of the CoFe-SFM fuel electrode (Fig. 3b) under the same condition. For example, at 800°C, the fuel electrode performance is promoted by 51% after reduction and exsolution, which implies that the CO/CO_2 conversion kinetics is greatly improved in practical single cells.

The Nyquist plots in EIS can be considered a "superposition" of a series of electrode processes that occur on the electrode. It is very challenging to identify the overlapped arcs using conventional Bode plots with lower resolution [52,53]. To determine the improvement mechanism of the CO/CO_2 conversion activity on the phase-transformed CoFe-SFM fuel electrode, a DRT method was utilized by deconvoluting EIS data [35]. Different electrode processes can be effectively separated with a

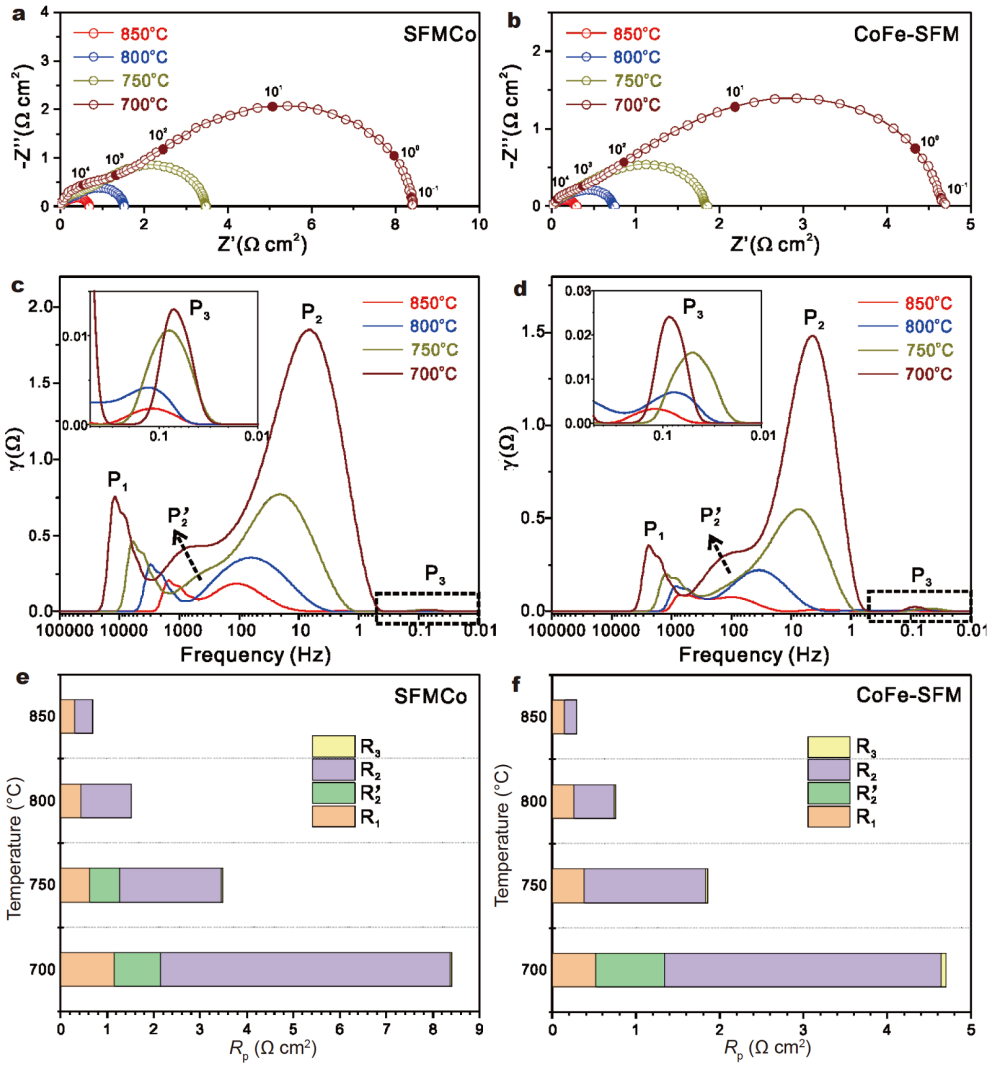

Figure 4 Electrochemical performance comparison of (a, c, e) SFMCo and (b, d, f) CoFe-SFM fuel electrodes in a 2:1 CO-CO_2 atmosphere at 700–850°C. (a, b) Nyquist plots, (c, d) DRT profiles, and (e, f) fitted resistance values of the identified peaks.

high resolution based on the respective characteristic frequencies. As shown in Fig. 4c, the response for the SFMCo fuel electrode is mainly contributed by two peaks (P_1 and P_2) at 800 and 850°C, whereas the third peak P_3 shows a negligible effect. The CoFe-SFM fuel electrode exhibits similar results at 750–850°C (Fig. 4d). However, a new peak P'_2 appears between P_1 and P_2 at 750 and 700°C for the SFMCo fuel electrode, while it appears at 700°C for the CoFe-SFM fuel electrode. Based on the predefined evaluation of EIS plots by the DRT curves, equivalent circuit models (ECMs) were determined, e.g., three series (R//CPE) circuits at 750–850°C and four series (R//CPE) circuits at 700°C for the CoFe-SFM fuel electrode. Each (R_i//CPE_i) circuit model represents a possible electrode substep, while R and CPE are the resistor and constant-phase element, respectively.

In Fig. 4a, b, the Nyquist plots were fitted using the complex nonlinear least-square method in Z-view software to obtain a series of resistance values, which correspond to the identified peaks in Fig. 4c, d, as summarized in Table S1 and shown in Fig. 4e, f. At 800°C, R_1 and R_2 are largely reduced from 0.440 and 1.074 Ω cm^2 for the SFMCo fuel electrode (Fig. 4e) to 0.258 and 0.476 Ω cm^2 for the CoFe-SFM fuel electrode (Fig. 4f). However, the negligible R_3 increases from 0.009 to 0.016 Ω cm^2. At 700°C, the first two peaks (R_1 and R_2) are also largely reduced from 1.156 to 0.520 Ω cm^2 for R_1 and from 6.221 to 3.303 Ω cm^2 for R_2. For the additional R'_2, the value is

slightly reduced from 0.995 to 0.816 Ω cm^2. In the meanwhile, R_3 increases from 0.03 to 0.06 Ω cm^2 at 700°C. Based on these impartial data, the high-resolution DRT method provides further insight into the resistance improvement on the phase-transformed CoFe-SFM fuel electrode.

In Fig. 4c, d, both P_1 and P_2 are significantly decreased and thermally activated. As suggested by the Adler-Lane-Steele model [54,55] and our previous work [37,43], P_1 at high frequency is correlated with the oxygen transport across the electrolyte (YSZ)-buffer layer (SDC), interface-fuel electrode interface (CoFe-SFM) and solid-state diffusion through the fuel electrode bulk. The improvement of P_1 may imply that SDC and SFM were deeply reduced during annealing in hydrogen. P_2 at medium frequency is assigned to the polarization loss of the CO/CO_2 conversion reaction on the fuel electrode surface, which consists of the electron transfer, surface oxygen exchange, and CO_2 dissociation/CO binding to O^* at the gas-electrode interface. The significant decrease of P_2 is entirely due to the phase-transformed fuel electrode, which consists of CoFe alloy with excellent activity and SFM with abundant oxygen vacancies and interstitial oxygen ions (Fig. S1a). The reaction active sites were expanded from the SFM surface to the gas-CoFe-SFM interface. Since the virtually negligible P_3 is located at low frequency (≤ 0.1 Hz), it can be undoubtedly ascribed to gas diffusion. The larger values for CoFe-SFM than the SFMCo fuel electrode can be explained by the slight difference in the porosity of these two electrodes. Interestingly, P'_2 appears at temperatures below 750°C for the SFMCo fuel electrode but 800°C for the CoFe-SFM fuel electrode. As a shoulder peak, it appears to be separated from P_2. The effective capacitance of P'_2 for the CoFe-SFM fuel electrode is calculated to be approximately 9×10^{-4} F, which is associated with the charge transfer (10^{-4}–10^{-5} F) for the oxygen exchange process [56]. This value is reasonable because electron-rich CoFe alloy is exsolved on the SFM surface, which increases the local electronic conductivity [51]. Through the above analysis and attribution, these four different

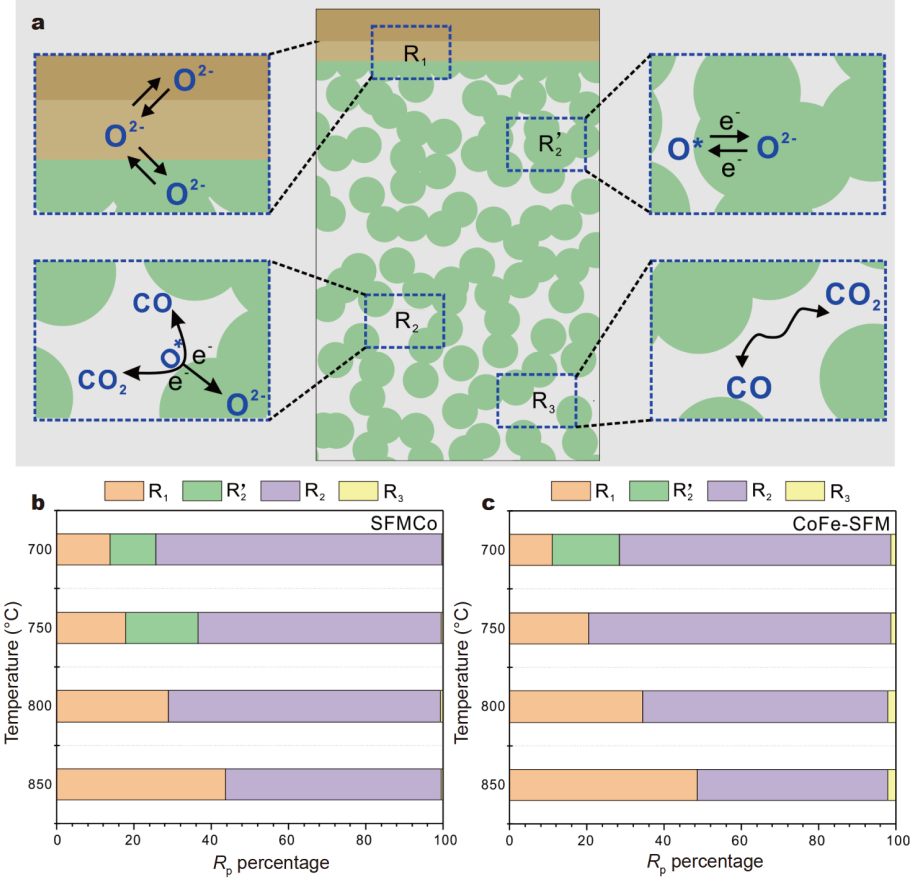

Figure 5 (a) Schematic diagram of four polarization processes in the fuel electrode towards the CO_2/CO conversion. (b, c) Calculated proportions of four polarization resistances in the SFMCo and CoFe-SFM fuel electrodes.

electrode substeps towards the CO/CO_2 conversion reaction are depicted in Fig. 5a. Therefore, it is evident from our comparative study that the phase-transformed fuel electrode can accelerate both surface/interface conversion kinetics and bulk oxygen transport processes except for gas diffusion.

To understand how the contribution of each substep evolves relative to one another with decreasing temperature, the percentages of four resistances to the total resistance were calculated, as summarized in Table S2 and shown in Fig. 5b, c. For the SFMCo fuel electrode (Fig. 5b), R_2 accounts for the largest proportion at all operating temperatures (55.90% at 850°C, 70.52% at 800°C, 62.88% at 750°C and 74.04% at 700°C, Table S2), which indicates that the CO/CO_2 conversion reaction remains limited by the surface kinetics. For the CoFe-SFM fuel electrode in Fig. 5c, similar results are observed at 700–800°C (63.47% at 800°C, 78.28% at 750°C and 70.30% at 700°C as shown in Table S2). At 850°C, R_1 (48.63%) and R_2 (49.32%) are almost equal, which indicates that the CO/CO_2 conversion reaction is colimited by the oxygen transport/diffusion and surface kinetics for the CoFe-SFM fuel electrode. Therefore, to achieve sufficiently enhanced electrode activity and reduce the operating temperature, modifying the active sites of the electrode surface is considered the most efficient method.

Fig. 6a depicts the schematic operating principle under the SOFC mode, which demonstrates the generation of electrical power by the oxidation of CO to CO_2. Furthermore, Fig. 6b shows the schematic operating principle under the SOEC mode, which highlights the storage of electrical power in CO from CO_2 reduction. Evidently, both CO oxidation reactions and CO_2 reduction reactions occur at the fuel electrode. To clarify the significance of our phase-transformed fuel electrode, a single cell supported on the YSZ electrolyte was fabricated (SEM images in Fig. S2a). In Fig. 3b, microsized SFMCo particles before reduction are interconnected with one another to form a continuous pathway for electron-ion transportation while showing a rounded and smooth surface. After the phase-transformation into CoFe-SFM (confirmed by the XRD pattern in Fig. 2b) in hydrogen, the electrode surface becomes rough (Fig. S2c). Well dispersed CoFe alloy nanoparticles appear over the micron-sized SFM grains (Fig. S2d), which successfully indicates the catalytic capability of our desired fuel electrode. In this case, the single cell is operated using a 2:1 $CO\text{-}CO_2$ mixture fed to the fuel electrode and LSM-SDC oxygen electrode in

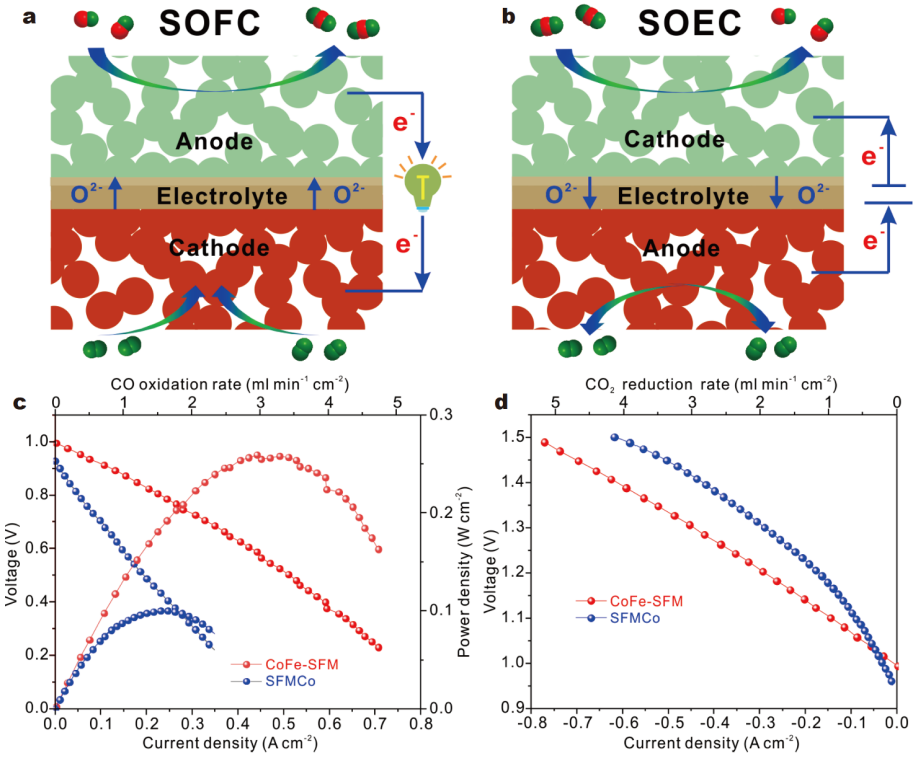

Figure 6 (a, b) Schematic of the (a) SOFC mode for CO oxidation and (b) SOEC mode for CO_2 reduction. (c, d) Comparison of the electrochemical performance of the CoFe-SFM cell and SFMCo cell at 800°C under the (c) SOFC mode and (d) SOEC mode.

ambient air. Fig. 6c compares the electrochemical performances of the CoFe-SFM- and SFMCo-based cells under the SOFC mode at 800°C. The positive current density represents the generated electricity when CO fuels are oxidized into CO_2. Before the reduction, the cell with the SFMCo fuel electrode shows a maximum power density (MPD) of approximately ~100 mW cm^{-2}. After full annealing in hydrogen and the feeding gas has been switched back to 2:1 CO-CO_2, the cell with the SFMCo fuel electrode shows an increased MPD of approximately 259 mW cm^{-2} by a factor of ~1.5. The cell also displays appreciable MPDs of 194 and 136 mW cm^{-2} at 750 and 700°C, respectively (Fig. S3). We calculated the corresponding CO conversion rate at 800°C, assuming a 100% current efficiency because of the unity ionic transport number in YSZ; it increased from 1.644 to 3.079 mL min^{-1} cm^{-2}. Fig. 6d compares the electrochemical performance under the SOEC mode at 800°C. The negative current density suggests the electricity energy storage as CO_2 is decomposed into CO and O_2. The cell with the CoFe-SFM fuel electrode achieves a current density of −0.453 A cm^{-2} at 1.3 V, which is much higher than that of the cell with the SFMCo fuel electrode (−0.291 A cm^{-2}) under identical operating voltage condition. The corresponding CO_2 conversion rate increases by 55.67% from 2.027 to 3.155 mL min^{-1} cm^{-2}. The cell also outputs good current densities of −0.350 and −0.226 A cm^{-2} at 1.3 V at 750 and 700°C, respectively (Fig. S3). Thus, this considerable enhancement of CO oxidation and CO_2 reduction kinetics is entirely attributed to a synergy effect between highly active CoFe alloy and SFM with abundant defects [57]. Since the electrolyte and oxygen electrode do not change in either cell, the considerably improved performance suggests the superiority of the CoFe-SFM fuel electrode.

To demonstrate the reversible operation between SOFC and SOEC modes, the single cell was examined at 800°C using two switching voltages: a voltage of 1.3 V higher than OCV for the CO_2 reduction and a lower voltage of 0.6 V for the CO oxidation. As shown in Fig. 7a, first, the cell was operated under a constant voltage of 1.3 V (SOEC mode) for 5 min to generate CO. Subsequently, the cell was instantly switched to the SOFC mode using a constant voltage of 0.6 V for the same duration. The

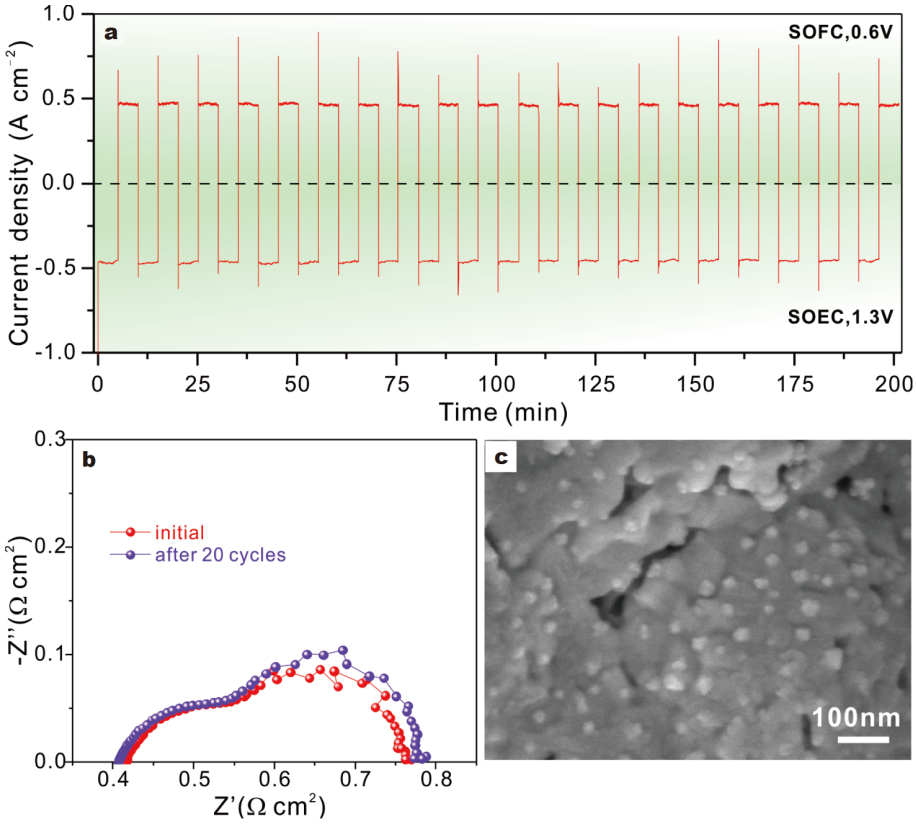

Figure 7 (a) Reversible 20-cycle test performance at 0.6 V (SOFC mode) and 1.3 V (SOEC mode); (b) EIS plots before and after the reversible cycle test; (c) high-resolution SEM image of the CoFe-SFM fuel electrode after the test.

stable current densities in each SOEC-SOFC cycle suggest that the reversible operation did not cause a significant negative effect on the performance of our cell with the CoFe-SFM fuel electrode. Fig. 7b compares the Nyquist plots under OCV conditions before and after the 20-cycle test, which shows no apparent change. Furthermore, the cell was broken into small pieces for the post-SEM characterization. In Fig. 7c, exsolved CoFe nanoparticles remain uniformly anchored on the SFM substrate without much agglomeration. Carbon deposition was not observed either. These two points prove that CoFe-SFM is an excellent fuel electrode with good durability, good carbon resistance, and successful CO/CO_2 conversion in RSOC. Thus, it has enormous potential for utilizing and storing renewable energy and yielding valuable chemicals.

CONCLUSIONS

We have demonstrated that the phase-transformed CoFe-SFM composite material can be developed as an efficient fuel electrode for RSOC. Both EIS and DRT studies suggest that the CO/CO_2 conversion performance was significantly improved by accelerating the bulk oxygen diffusion and surface reaction kinetics on the CoFe-SFM fuel electrode, which improved the CO_2 reduction rate by 55.67%@1.3 V and CO oxidation rate by 150% at 800°C compared with the control sample. Moreover, RSOCs with the CoFe-SFM electrode demonstrated excellent cyclability and durability in 20 cycle operations. Therefore, this study may provide future guidance for designing fuel electrodes and utilizing RSOC for efficient CO_2 conversion and utilization. A long reversible operation is required and currently performed in the lab, and the result will be reported soon.

Received 12 June 2020; accepted 28 September 2020; published online 28 December 2020

1 Mogensen MB, Chen M, Frandsen HL, *et al.* Reversible solid-oxide cells for clean and sustainable energy. Clean Energy, 2019, 3: 175–201
2 Ding H, Wu W, Jiang C, *et al.* Self-sustainable protonic ceramic electrochemical cells using a triple conducting electrode for hydrogen and power production. Nat Commun, 2020, 11: 1907
3 Yang D, Wang G, Wang X. Photo- and thermo-coupled electrocatalysis in carbon dioxide and methane conversion. Sci China Mater, 2019, 62: 1369–1373
4 Irvine JTS, Neagu D, Verbraeken MC, *et al.* Evolution of the electrochemical interface in high-temperature fuel cells and electrolysers. Nat Energy, 2016, 1: 15014
5 Wang Y, Liu T, Lei L, *et al.* High temperature solid oxide H_2O/CO_2 co-electrolysis for syngas production. Fuel Processing Tech, 2017, 161: 248–258
6 Da'as EH, Bi L, Boulfrad L, *et al.* Nanostructuring the electronic conducting $La_{0.8}Sr_{0.2}MnO_{3-\delta}$ cathode for high-performance in proton-conducting solid oxide fuel cells below 600°C. Sci China Mater, 2018, 61: 57–64
7 Liu T, Chen X, Wu J, *et al.* A highly-performed, dual-layered cathode supported solid oxide electrolysis cell for efficient CO_2 electrolysis fabricated by phase inversion Co-tape casting method. J Electrochem Soc, 2017, 164: F1130–F1135
8 Skafte TL, Blennow P, Hjelm J, *et al.* Carbon deposition and sulfur poisoning during CO_2 electrolysis in nickel-based solid oxide cell electrodes. J Power Sources, 2018, 373: 54–60
9 Wang Y, Liu T, Fang S, *et al.* Syngas production on a symmetrical solid oxide H_2O/CO_2 co-electrolysis cell with $Sr_2Fe_{1.5}Mo_{0.5}O_6$–$Sm_{0.2}Ce_{0.8}O_{1.9}$ electrodes. J Power Sources, 2016, 305: 240–248
10 Park S, Han H, Yoon W, *et al.* Improving a sulfur-tolerant Ruddlesden–Popper catalyst by fluorine doping for CO_2 electrolysis reaction. ACS Sustain Chem Eng, 2020, 8: 6564–6571
11 Ebbesen SD, Mogensen M. Electrolysis of carbon dioxide in solid oxide electrolysis cells. J Power Sources, 2009, 193: 349–358
12 Yan J, Chen H, Dogdibegovic E, *et al.* High-efficiency intermediate temperature solid oxide electrolyzer cells for the conversion of carbon dioxide to fuels. J Power Sources, 2014, 252: 79–84
13 Yue X, Irvine JTS. Modification of LSCM–GDC cathodes to enhance performance for high temperature CO_2 electrolysis using solid oxide electrolysis cells (SOECs). J Mater Chem A, 2017, 5: 7081–7090
14 Zhang L, Hu S, Li W, *et al.* Nano-CeO_2-modified cathodes for direct electrochemical CO_2 reduction in solid oxide electrolysis cells. ACS Sustain Chem Eng, 2019, 7: 9629–9636
15 Ye L, Hu X, Wang X, *et al.* Enhanced CO_2 electrolysis with a $SrTiO_3$ cathode through a dual doping strategy. J Mater Chem A, 2019, 7: 2764–2772
16 Li Y, Chen X, Yang Y, *et al.* Mixed-conductor $Sr_2Fe_{1.5}Mo_{0.5}O_{6-\delta}$ as robust fuel electrode for pure CO_2 reduction in solid oxide electrolysis cell. ACS Sustain Chem Eng, 2017, 5: 11403–11412
17 Rabuni MF, Vatcharasuwan N, Li T, *et al.* High performance micro-monolithic reversible solid oxide electrochemical reactor. J Power Sources, 2020, 458: 228026
18 Connor PA, Yue X, Savaniu CD, *et al.* Tailoring SOFC electrode microstructures for improved performance. Adv Energy Mater, 2018, 8: 1800120
19 Zhao C, Li Y, Zhang W, *et al.* Heterointerface engineering for enhancing the electrochemical performance of solid oxide cells. Energy Environ Sci, 2020, 13: 53–85
20 Ling Y, Wang Z, Wang Z, *et al.* A robust carbon tolerant anode for solid oxide fuel cells. Sci China Mater, 2015, 58: 204–212
21 Gong M, Dai H. A mini review of NiFe-based materials as highly active oxygen evolution reaction electrocatalysts. Nano Res, 2015, 8: 23–39
22 Khan WU, Chen SS, Tsang DCW, *et al.* Catalytically active interfaces in titania nanorod-supported copper catalysts for CO oxidation. Nano Res, 2020, 13: 533–542
23 Yang C, Yang Z, Jin C, *et al.* Sulfur-tolerant redox-reversible anode material for direct hydrocarbon solid oxide fuel cells. Adv Mater, 2012, 24: 1439–1443
24 Sun YF, Zhang YQ, Chen J, *et al.* New opportunity for *in situ* exsolution of metallic nanoparticles on perovskite parent. Nano Lett, 2016, 16: 5303–5309
25 Neagu D, Tsekouras G, Miller DN, *et al. In situ* growth of nanoparticles through control of non-stoichiometry. Nat Chem, 2013, 5: 916–923

26 Zhu Y, Zhou W, Ran R, *et al.* Promotion of oxygen reduction by exsolved silver nanoparticles on a perovskite scaffold for low-temperature solid oxide fuel cells. Nano Lett, 2016, 16: 512–518
27 Du Z, Zhao H, Yi S, *et al.* High-performance anode material $Sr_2FeMo_{0.65}Ni_{0.35}O_{6-\delta}$ with *in situ* exsolved nanoparticle catalyst. ACS Nano, 2016, 10: 8660–8669
28 Zhang T, Zhao Y, Zhang X, *et al.* Thermal stability of an *in situ* exsolved metallic nanoparticle structured perovskite type hydrogen electrode for solid oxide cells. ACS Sustain Chem Eng, 2019, 7: 17834–17844
29 Neagu D, Papaioannou EI, RamLi WKW, *et al.* Demonstration of chemistry at a point through restructuring and catalytic activation at anchored nanoparticles. Nat Commun, 2017, 8: 1855
30 Liu S, Liu Q, Luo JL. CO_2-to-CO conversion on layered perovskite with *in situ* exsolved Co–Fe alloy nanoparticles: an active and stable cathode for solid oxide electrolysis cells. J Mater Chem A, 2016, 4: 17521–17528
31 Qiu P, Yang X, Wang W, *et al.* Redox-reversible electrode material for direct hydrocarbon solid oxide fuel cells. ACS Appl Mater Interfaces, 2020, 12: 13988–13995
32 Yang C, Li J, Lin Y, *et al. In situ* fabrication of CoFe alloy nanoparticles structured $(Pr_{0.4}Sr_{0.6})_3(Fe_{0.85}Nb_{0.15})_2O_7$ ceramic anode for direct hydrocarbon solid oxide fuel cells. Nano Energy, 2015, 11: 704–710
33 Hu B, Wang Y, Xia C. Effects of ceria conductivity on the oxygen incorporation at the LSCF-SDC-gas three-phase boundary. J Electrochem Soc, 2015, 162: F33–F39
34 Chen L, Chen F, Xia C. Direct synthesis of methane from CO_2–H_2O co-electrolysis in tubular solid oxide electrolysis cells. Energy Environ Sci, 2014, 7: 4018–4022
35 Wan TH, Saccoccio M, Chen C, *et al.* Influence of the discretization methods on the distribution of relaxation times deconvolution: implementing radial basis functions with DRTtools. Electrochim Acta, 2015, 184: 483–499
36 Saccoccio M, Wan TH, Chen C, *et al.* Optimal regularization in distribution of relaxation times applied to electrochemical impedance spectroscopy: ridge and lasso regression methods—A theoretical and experimental study. Electrochim Acta, 2014, 147: 470–482
37 Li Y, Hu B, Xia C, *et al.* A novel fuel electrode enabling direct CO_2 electrolysis with excellent and stable cell performance. J Mater Chem A, 2017, 5: 20833–20842
38 Zheng K, Świerczek K, Polfus JM, *et al.* Carbon deposition and sulfur poisoning in $SrFe_{0.75}Mo_{0.25}O_{3-\delta}$ and $SrFe_{0.5}Mn_{0.25}Mo_{0.25}O_{3-\delta}$ electrode materials for symmetrical SOFCs. J Electrochem Soc, 2015, 162: F1078–F1087
39 Xi X, Cao ZS, Shen XQ, *et al. In situ* embedding of CoFe nanocatalysts into Sr_3FeMoO_7 matrix as high-performance anode materials for solid oxide fuel cells. J Power Sources, 2020, 459: 228071
40 Lv H, Lin L, Zhang X, *et al. In situ* investigation of reversible exsolution/dissolution of CoFe alloy nanoparticles in a Co-doped $Sr_2Fe_{1.5}Mo_{0.5}O_{6-\delta}$ cathode for CO_2 electrolysis. Adv Mater, 2020, 32: 1906193
41 Gao Y, Chen D, Saccoccio M, *et al.* From material design to mechanism study: Nanoscale Ni exsolution on a highly active A-site deficient anode material for solid oxide fuel cells. Nano Energy, 2016, 27: 499–508
42 Neagu D, Oh TS, Miller DN, *et al.* Nano-socketed nickel particles with enhanced coking resistance grown *in situ* by redox exsolution. Nat Commun, 2015, 6: 8120
43 Li Y, Li Y, Wan Y, *et al.* Perovskite oxyfluoride electrode enabling direct electrolyzing carbon dioxide with excellent electrochemical performances. Adv Energy Mater, 2019, 9: 1803156
44 Lv H, Lin L, Zhang X, *et al. In situ* exsolved $FeNi_3$ nanoparticles on nickel doped $Sr_2Fe_{1.5}Mo_{0.5}O_{6-\delta}$ perovskite for efficient electrochemical CO_2 reduction reaction. J Mater Chem A, 2019, 7: 11967–11975
45 Zhu Z, Li M, Xia C, *et al.* Bismuth-doped $La_{1.75}Sr_{0.25}NiO_{4+\delta}$ as a novel cathode material for solid oxide fuel cells. J Mater Chem A, 2017, 5: 14012–14019
46 Chroneos A, Yildiz B, Tarancón A, *et al.* Oxygen diffusion in solid oxide fuel cell cathode and electrolyte materials: mechanistic insights from atomistic simulations. Energy Environ Sci, 2011, 4: 2774–2789
47 Sahai A, Goswami N. Probing the dominance of interstitial oxygen defects in ZnO nanoparticles through structural and optical characterizations. Ceramics Int, 2014, 40: 14569–14578
48 Fan HB, Yang SY, Zhang PF, *et al.* Investigation of oxygen vacancy and interstitial oxygen defects in ZnO films by photoluminescence and X-ray photoelectron spectroscopy. Chin Phys Lett, 2007, 24: 2108–2111
49 Ma X, Carneiro JSA, Gu XK, *et al.* Engineering complex, layered metal oxides: High-performance nickelate oxide nanostructures for oxygen exchange and reduction. ACS Catal, 2015, 5: 4013–4019
50 Hu X, Li M, Xie Y, *et al.* Oxygen-deficient Ruddlesden–Popper-type lanthanum strontium cuprate doped with bismuth as a cathode for solid oxide fuel cells. ACS Appl Mater Interfaces, 2019, 11: 21593–21602
51 Meng X, Wang Y, Zhao Y, *et al. In-situ* exsolution of nanoparticles from Ni substituted $Sr_2Fe_{1.5}Mo_{0.5}O_6$ perovskite oxides with different Ni doping contents. Electrochim Acta, 2020, 348: 136351
52 Schichlein H, Müller AC, Voigts M, *et al.* Deconvolution of electrochemical impedance spectra for the identification of electrode reaction mechanisms in solid oxide fuel cells. J Appl Electrochem, 2002, 32: 875–882
53 Zhang Y, Chen Y, Yan M, *et al.* Reconstruction of relaxation time distribution from linear electrochemical impedance spectroscopy. J Power Sources, 2015, 283: 464–477
54 Adler SB. Factors governing oxygen reduction in solid oxide fuel cell cathodes. Chem Rev, 2004, 104: 4791–4844
55 Adler SB, Lane JA, Steele BCH. Electrode kinetics of porous mixed-conducting oxygen electrodes. J Electrochem Soc, 1996, 143: 3554–3564
56 Oz A, Singh K, Gelman D, *et al.* Understanding of oxygen reduction reaction on perovskite-type $Ba_{0.5}Sr_{0.5}Fe_{0.91}Al_{0.09}O_{3-\delta}$ and $Ba_{0.5}Sr_{0.5}Fe_{0.8}Cu_{0.2}O_{3-\delta}$ using AC impedance spectroscopy genetic programming. J Phys Chem C, 2018, 122: 15097–15107
57 Ye L, Zhang M, Huang P, *et al.* Enhancing CO_2 electrolysis through synergistic control of non-stoichiometry and doping to tune cathode surface structures. Nat Commun, 2017, 8: 14785

Acknowledgements This work was financially supported by the National Natural Science Foundation (52002249, 51402093 and 21706162), Guangdong Basic and Applied Basic Research Foundation (2019A1515110025 and 2017A 030313289), the Research Grant for Scientific Platform and Project of Guangdong Provincial Education Office (2019KTSCX151), China Postdoctoral Science Foundation (2020M682872) and Shenzhen Government's Plan of Science and Technology (JCYJ20180305125247308). Technical support from the Instrumental Analysis Center of Shenzhen University (Xili Campus) is

also appreciated.

Author contributions Fan L and Li Y conceived the idea, designed the experiments, analyzed the data and wrote the manuscript. Singh M and Zhuang Z performed the material microstructure characterization. Jing Y and Maliutina K participated in device optimization and data analysis. Li Y drafted the manuscript. He C and Fan L contributed to the final version of the manuscript. All authors contributed to the general discussion and reviewed the manuscript.

Conflict of interest The authors declare that they have no conflict of interest.

Supplementary information The XPS O 1s spectra, SEM images of typical cells, the temperature dependence of RSOC electrochemical performance, EIS fitting and DRT deconvolution results are available in the online version of the paper.

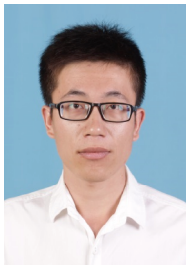

Yihang Li received his PhD in materials science from the University of Science and Technology of China (USTC) in 2019. In 2019, he joined Dr. Fan's group as a postdoc at Shenzhen University. His main research focuses on rational design and fabrication of novel perovskite materials as electrodes for solid oxide fuel/electrolysis cells.

Liangdong Fan received his PhD one in energy technology from the Royal Institute of Technology (KTH, Sweden) in 2014 and another in chemical technology from Tianjin University in 2012. In 2015, Dr. Fan joined Shenzhen University as a Lecturer/Research Associate Professor (Principal Investigator). His current research interests are developing inorganic functional materials such as perovskite oxides for high-temperature fuel cells and low-temperature electrocatalysis applications.

相变燃料电极实现固体氧化物电池高效可逆CO/CO_2转化

李一航[1,2], Manish Singh[3], 庄泽超[4], 景义甫[1], 李凤姣[1], Kristina Maliutina[1], 何传新[1], 范梁栋[1,5*]

摘要 固体氧化物电池可实现CO/CO_2的可逆转化，在电能和化学能相互转化过程中显示出巨大潜力. 然而，其商业化进展一直受到燃料极抗积碳性能差的限制. 本工作中，我们发展了一种CoFe合金纳米颗粒和Ruddlesden-Popper层状结构$Sr_3Fe_{1.25}Mo_{0.75}O_{7-\delta}$复合新型燃料电极(CoFe-SFM)，其可以通过钙钛矿$Sr_2Fe_{7/6}Mo_{0.5}Co_{1/3}O_{6-\delta}$在还原气氛中退火发生相变得到. 电化学阻抗谱和弛豫时间分步法分析可知CoFe-SFM电极通过改善体相氧化学扩散能力和表面氧交换过程来增强CO氧化和CO_2还原动力学. 在固体氧化物燃料电池模式下，800°C的最大功率达到259 mW cm^{-2}；在固体氧化物电解电池模式下，1.3 V工作电压下单电池的电解电流密度为−0.453 A cm^{-2}，都远超对比电极材料. 在20次SOFC-SOEC循环操作条件下，CoFe-SFM燃料极依然保持稳定的微结构和抗积碳性能，电池性能保持良好. 该工作可为CO_2转化、抗积碳电极材料设计和提升电极表界面反应动力学提供一定的指导作用.

